BILINGUAL PUBLISHING GROUP

Non-Metallic Material Science

https://journals.bilpubgroup.com/index.php/nmms

ARTICLE

Synthesis, Characterization and Impedance Analysis of Calcium-Doped Zinc Oxide Nanoparticles

K. N. Ganesha[1,2], H. Chandrappa[2], S. R. Kumarswamy[3], V. Annadurai[4], H. Somashekarappa[1*], R. Somashekar[5]

[1] *Department of Physics, Yuvaraja's College, University of Mysore, Mysuru, Karnataka, 570005, India*

[2] *SRSMN Govt. First Grade College & PG Study Centre, Barkur, Udupi, Karnataka, 576210, India*

[3] *Government First Grade College for Women, Byrapura, T. Narasipura, Mysuru, Karnataka, 571124, India*

[4] *Department of Physics, NIE First Grade College, University of Mysore, Mysuru-570008, India*

[5] *Institution of Excellence, Vijnana Bhavana, Manasagangothri, Mysuru, 570006, India*

ABSTRACT

The calcium-doped ZnO nanoparticles, $Zn_{1-x}Ca_xO$ (x = 0, 0.025, 0.05, 0.075) were prepared by the solution combustion method. The synthesized nanoparticles were characterized by various techniques such as XRD, FTIR, Raman, FESEM-EDX, PL, Impedance, and UV-Vis. The Rietveld refinement of the X-ray diffractogram yields the crystalline structure and lattice parameters. Also, the XRD analysis shows that the substitution of Ca into ZnO does not alter the Wurtzite structure of ZnO. The crystallite size of the samples, calculated using the Scherer equation, was found to be between 46 nm and 92 nm. FTIR spectra detect the ZnO-related vibration modes of the samples. The FESEM morphological images suggest the spherical shape of the synthesized nanoparticles. The EDAX spectra identify the presence of Zn, Ca, and O atoms in the samples. The Raman active modes of the ZnO phase were identified by Raman spectral analysis. The analysis of Photoluminescence (PL) spectra gives information about the UV emission and other visible bands corresponding to violet, blue, and green emission representing different intrinsic defects in synthesized nanoparticles. Using UV-vis spectroscopy, the optical transparency and band gap values were examined. The energy band gap obtained by Tauc's plot was decreased with the increase in Ca doping. Impedance analysis shows that the grain conductivity increased with the increase in dopant concentration. Contrarily, the total conductivity decreased with the increasing doping concentration due to increased grain boundary resistance. The proposed work demonstrates the changes in microstructure, electrical conductivity, and optical bandgap energy with Ca-doping. These synthesized Ca-doped ZnO nanoparticles could be promising materials for photocatalytic applications.

Keywords: Solution combustion synthesis; ZnO; Impedance; Optical properties; Photoluminescence

*CORRESPONDING AUTHOR:

H. Somashekarappa, Department of Physics, Yuvaraja's College, University of Mysore, Mysuru, Karnataka, 570005, India; Email: drhssappa@gmail.com

ARTICLE INFO

Received: 22 April 2023 | Revised: 15 May 2023 | Accepted: 16 May 2023 | Published Online: 25 May 2023

DOI: https://doi.org/10.30564/nmms.v5i1.5677

CITATION

Ganesha, K.N., Chandrappa, H., Kumarswamy, S.R., et al., 2023. Synthesis, Characterization and Impedance Analysis of Calcium Doped Zinc Oxide Nanoparticles. Non-Metallic Material Science. 5(1): 49-63. DOI: https://doi.org/10.30564/nmms.v5i1.5677

1. Introduction

As the most studied zinc oxide (ZnO), it offers some attractive properties due to its size-dependent optoelectronic properties. In recent days, ZnO has revolutionized the optoelectronics industry due to its interesting semiconducting, pyroelectric, and piezoelectric properties. ZnO has diverse applications such as gas/chemical sensors [1-3], optoelectronics [4], laser diodes [5], piezo electronics [6,7], photo-catalysis [8], food packaging [9], biomedical [10], personal care and cosmetics [11] and field emission devices [12]. Basically, ZnO (group II-VI) is a wide-bandgap semiconductor with unique physical properties. It has a direct band gap energy of 3.37 eV with a free exciton binding energy of 60 meV. Therefore, it has a pronounced effect on optical and electrical properties [13,14]. It is well established that particle size and morphology, reaction temperature, solution pH, dopants, and dopant concentrations alter the physical, chemical, electrical, and optical properties of ZnO [15-21]. ZnO nanoparticles can be obtained by various synthesis methods such as co-precipitation [22,23], combustion [24], sol-gel [25,26], hydrothermal [27], etc. Many researchers have synthesized Ca-doped ZnO, and the observed properties have been used in many applications. For example, Davalasab Ilager et al. modified a carbon-based electrochemical sensor with Ca-doped ZnO nanoparticles for an anti-viral drug, and acyclovir [28,29]. S. Jaballah et al. fabricated a Ca-doped zinc oxide gas sensor that exhibits good formaldehyde detection properties [30]. Here, the authors made an attempt to prepare the Ca-doped ZnO by solution combustion synthesis technique. This technique is preferred over other synthesis approaches on account of the major advantage that allows homogeneous phase formation at lower temperatures or at shorter reaction times than conventional methods such as solid-state and mechano-synthesis routes [31]. No extensive literature on the combination of electrical and optical properties and the nanocrystalline phase of this material. An idea about the charge carriers, bandgap energy, and electrical conductivity of this material is essential. The details of structural modifications with Ca doping on ZnO material have been obtained using Rietveld refinement from the XRD data. The principle objective of the current work is to investigate and discuss the influence of Ca doping on the structural, morphological, optical, and electrical properties of synthesized ZnO nanoparticles.

2. Experimental

2.1 Solution combustion synthesis

In a typical solution combustion synthesis, the metal nitrates act as oxidizing agents, and the organic fuels as the reducing agents [24,32]. To prepare $Zn_{1-x}Ca_xO$ (x = 0, 0.025, 0.05, 0.075), Zinc Nitrate Hexahydrate [$Zn(NO_3)_2 \cdot 6H_2O$] (99%), Calcium Nitrate Tetra hydrate [$Ca(NO_3)_2 \cdot 4H_2O$] (99.9%) were used as the precursor (oxidizing agent) and citric acid [$C_6H_8O_7$] (99%) as the fuel. All the chemicals used for the preparation are AR grade. The fuel and oxidant ratio was maintained at one during the preparation. 1 = O/(-n)F, where n is the fuel mole fraction, O is the oxidation valence, and F is the reduction valence [33]. The fuel mole fraction was calculated based on the valences of the oxidizing and reducing elements. Valences of elements like +1 for H, +4 for C, −2 for O, and 0 for N. Valences for metal elements like +2 for Zn and +2 for Ca. The oxidizing valence of $Zn(NO_3)_2 \cdot 6H_2O$ is −10, $Ca(NO_3)_2.4H_2O$ is −10, and the reducing valence of citric acid is +18. The amount of citric acid (fuel) calculated for the reaction is n = 0.56M.

Stoichiometric amounts of $Zn(NO_3)_2 \cdot 6H_2O$ and $Ca(NO_3)_2 \cdot 4H_2O$ and $C_6H_8O_7$ were dissolved in separate beakers with double distilled water. A clear solution of metal nitrates was intimately mixed in a beaker equipped with a magnetic stirrer until a clear solution was formed. Citric acid fuel was also dissolved in distilled water in a separate beaker with a magnetic stirrer until a clear solution was obtained. The above solutions were mixed then the resulting aqueous solution was thoroughly stirred with a magnetic stirrer at room temperature for about 30 minutes until a clear solution was formed. At low pH, nitrates reduce the enthalpy of the exothermic reaction under this condition and the particles agglomerate [34]. The

pH of the solution is maintained at 7 by adding ammonium hydroxide. By heating this mixture at 80 °C under constant stirring for 8 h, the excess water and nitrate gas were removed to form a transparent and viscous gel. Excess water and nitric acid gas were removed to form a clear, viscous gel. Further heating of the gel at 150 °C causes it to ignite and burn completely, forming a carbonaceous powder. The obtained powder material was allowed to cool and ground in an agate mortar to get a fine powder, then annealed at 800 °C for 6 hours to obtain phase pure calcium-doped zinc oxide nanoparticles.

2.2 Characterization

X-ray diffractogram (XRD) patterns were recorded using the X-ray Diffractometer (Bruker AXS D8 Advance) fitted with Cu-Kα radiation (λ = 1.5406 Å) to get structural information of the prepared nanoparticles. The vibrational modes of the samples were characterized using an FTIR spectrometer (Perkin Elmer Spectrum1) and a Raman spectrometer (LabRAM HR 800, HORIBA, excitation laser 532 nm). The surface morphology and elemental analysis of the samples were investigated by FESEM and EDAX (ΣIGMAZEISS FESEM). Optical absorption spectra were recorded over the wavelength range of 350-800 nm using an ultraviolet-visible-near-infrared (UV-VIS-NIR) spectrophotometer (Perkin Elmer UV Lambda 900). Photoluminescence (PL) was measured using HORIBA with a laser light excitation wavelength of 355 nm. Electrical impedance measurements were made at room temperature from 100 Hz to 1 MHz using a Wayne Kerr 6500B Precision Impedance Analyzer. The silver paste was applied evenly on both sides of the pellet to ensure good electrical contact.

3. Results and discussion

3.1 Structural analysis

Figure 1 shows the powder XRD patterns of samples prepared with $Zn_{1-x}Ca_xO$ (x = 0, 0.025, 0.05, 0.075) calcined at 800 °C. A hexagonal wurtzite structure with space group $P6_3mc$ (JCPDS01-075-0576) is evident from the XRD pattern. Ca^{2+} doping does not show any additional peaks in the diffractograms, confirming that Ca is perfectly incorporated into the ZnO matrix without altering the wurtzite structure. A negligible shift in peak positions towards lower 2θ values was observed with Ca doping. The shift to smaller angles was caused by the larger radius of the Ca^{2+} ion (0.99 Å) [23]. XRD diffractograms were examined with the Rietveld fitting using FullProf software. **Figure 2** shows the Rietveld refinement (Fullprof) of XRD pattern for ZnO (CA00), $Zn_{0.975}Ca_{0.025}O$ (CA25), $Zn_{0.95}Ca_{0.05}O$ (CA50) and $Zn_{0.925}Ca_{0.075}O$ (CA75) nanoparticles. **Table 1** illustrates the lattice and the Rietveld parameters χ^2 (reduced chi-square) obtained by the Rietveld fit. The χ^2 values of the samples vary between 1.42 and 3.42, which justifies the goodness of refinement. All samples converge to a hexagonal wurtzite structure of space group $P6_3mc$. In the Wurtzite structure, Zn^{2+} is bonded to four equivalent O^{2-} atoms to form a corner-sharing ZnO_4 tetrahedra. Although Ca ions occupy regular lattice sites in ZnO, variations in lattice parameter values produce crystal defects around the dopants, and it has been suggested that these defects change the stoichiometry of the material.

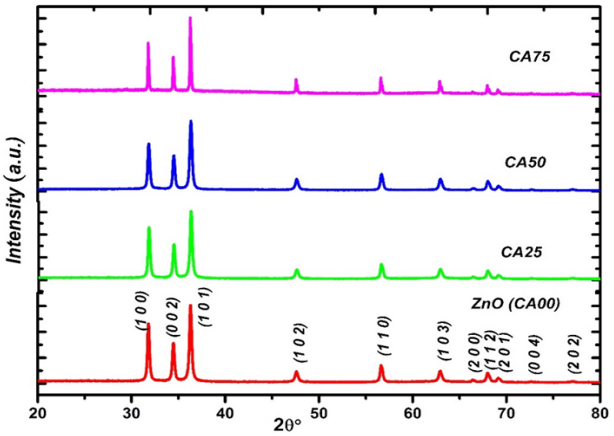

Figure 1. XRD pattern of ZnO (CA00), $Zn_{0.975}Ca_{0.025}O$ (CA25), $Zn_{0.95}Ca_{0.05}O$ (CA50), and $Zn_{0.925}Ca_{0.075}O$ (CA75) nanoparticles calcined at 800 °C.

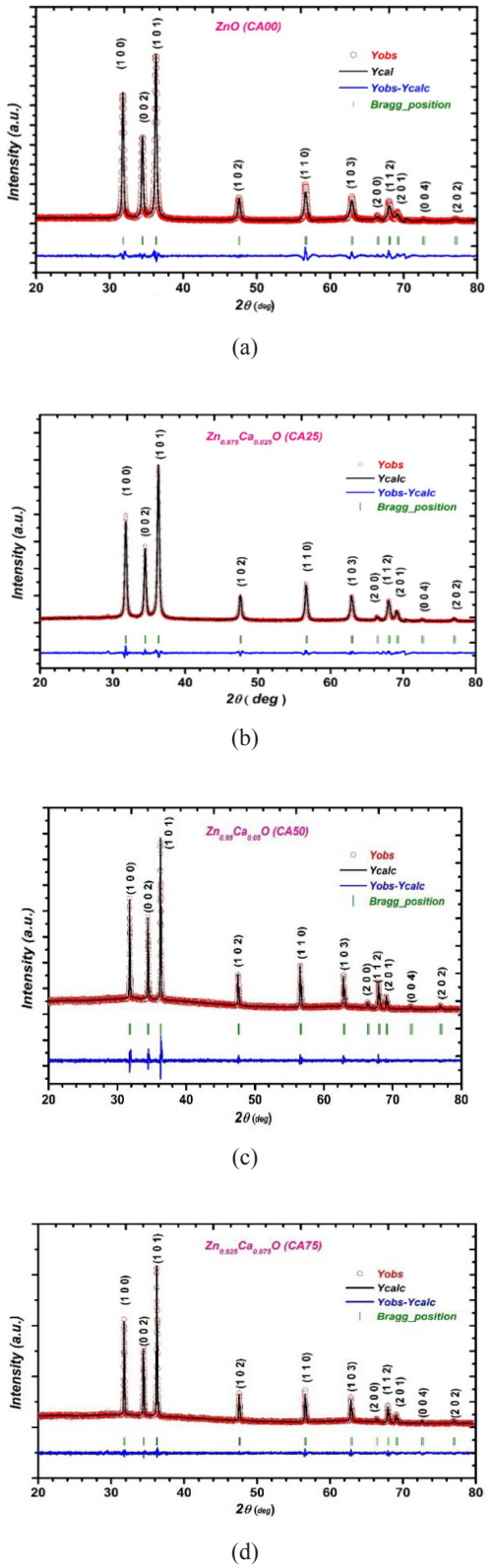

Figure 2. Rietveld fit of pure and Ca-doped ZnO nanoparticles (a) ZnO (CA00), (b) $Zn_{0.975}Ca_{0.025}O$ (CA25), (c) $Zn_{0.95}Ca_{0.05}O$ (CA50) and (d) $Zn_{0.925}Ca_{0.075}O$ (CA75).

The average crystallite size (D) is estimated using Debye-Scherrer's equation [35] as follows:

$$D = \frac{K\lambda}{\beta \cos\theta} \quad (1)$$

where D is the average crystallite size, K is a constant (0.9), λ is the wavelength of X-rays, β is the full width at half maxima (FWHM) of a (101) reflection peak, and θ is the Bragg's diffraction angle.

The calculated crystallite size values are shown in **Table 1**. The average crystallite size was found to be the smallest (42 nm) for CA25 and the largest (92 nm) for CA75. This indicates that the average crystallite size increases with increasing dopant concentration. The bond length (L) of Zn-O was calculated from the relation [26]:

$$L = \sqrt{\frac{a^2}{3} + \left(\frac{1}{2} - u\right)^2 c^2} \quad (2)$$

where *a* and *c* are lattice constants and *u* is a positional parameter. The parameter *u* can be calculated by using the formula: $u=(a^2/3c^2)+0.25$. The calculated positional parameters and bond lengths are also shown in **Table 1**. It was observed that the bond length increased slightly with increasing Ca concentration.

3.2 Fourier Transform Infra-Red (FTIR) spectra analysis

The characteristics vibrational frequencies of $Zn_{1-x}Ca_xO$ nanoparticles with wurtzite structure were identified using FTIR spectra. **Figure 3** shows the FTIR spectra of the prepared samples. Infrared active optical phonon modes in ZnO were observed in the spectral range from 300 to 600 cm^{-1} [26,36]. The absorption peaks observed between 401-412 cm^{-1} can be assigned to the E_1 (TO) mode of pure and Ca-doped ZnO. The band 484 cm^{-1} can be assigned to the surface phonon mode A_1(TO). Two additional bands, 912 cm^{-1} and 1010 cm^{-1} were assigned to the vibrational frequencies due to the changes in the microstructural features by adding Ca into the ZnO lattice [37,38].

Table 1. XRD analysis results of ZnO and Ca-doped ZnO nanoparticles.

Sample	a=b (Å)	C (Å)	Atomic packing factor (c/a)	Volume $(Å)^3$	Average crystallite size D (nm)	χ^2	Bond length Zn-O L (Å)	Position parameters u
CA00	3.2482	5.2036	1.602	47.54	52	3.32	1.976	0.379
CA25	3.2479	5.2032	1.602	47.54	46	3.42	1.976	0.379
CA50	3.2505	5.2051	1.601	47.63	50	1.95	1.977	0.379
CA75	3.2504	5.2049	1.601	47.62	92	1.42	1.977	0.380

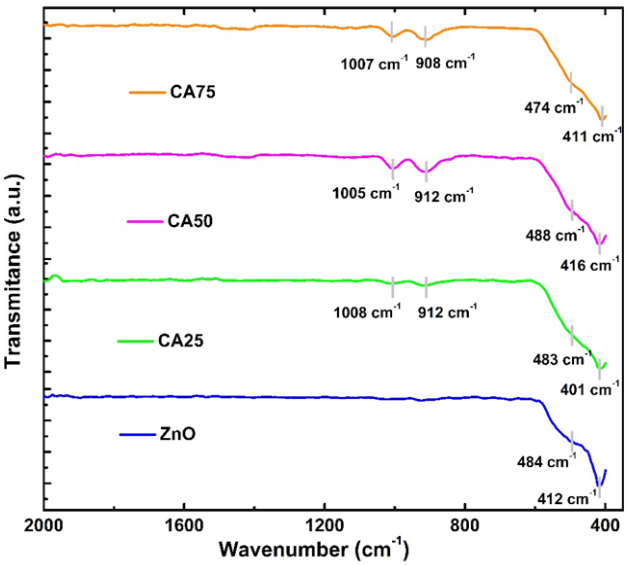

Figure 3. FTIR absorption spectra of pure ZnO and Ca-doped ZnO nanoparticles.

3.3 Raman analysis

The lattice vibrational properties of the prepared samples were studied by Raman spectroscopy. The prepared sample $Zn_{1-x}Ca_xO$ (x = 0. 0.025, 0.05, 0.075) crystallizes into a wurtzite structure with symmetry $P6_3mc$. Since there are four atoms per unit cell in the wurtzite structure, there are 12 phonon modes. Among 12 modes, three longitudinal-optical (LO), six transverse optical (TO) branches, one longitudinal-acoustic (LA), and two transverse-acoustic (TA). The irreducible representation for the zone-centre optical phonons is $G_{opt} = A_1 + E_1 + 2E_2 + 2B_1$ [39]. The B_1 mode is silent, the A_1 and E_1 modes are both Raman and infrared active, while the E_2 mode is non-polar and Raman-only active. Raman spectra were obtained at an excitation wavelength of 512 nm, as shown in **Figure 4**. The absorption peaks in **Table 2** are attributed to the 1st and 2nd-order Raman active modes of ZnO and Ca-doped ZnO. The two most intense peaks were associated with the nonpolar mode E_2. The E_2^{low} vibrational mode around 100 cm^{-1} corresponds to the vibrations of the zinc sublattice. Another intense vibrational mode E_2^{high} near 438 cm^{-1} corresponds to oxygen migration and is characteristic of the hexagonal wurtzite phase of ZnO [39-42]. The peaks at 334 cm^{-1} and 391 cm^{-1} correspond to the second-order Raman modes (multiple phonon processes) E_2^{high}-E_2^{low} and A_1 (TO) [42], respectively. The peak at 582 cm^{-1} is attributed to the E_1 (LO) vibrational mode. This mode implies the presence of structural defects due to oxygen vacancies, Zn interstitial atoms, and impurities [43]. The combined acoustic and optical vibrational modes A_1 (TA) and A_1 (LO) also occur between 651 cm^{-1} and 665 cm^{-1}.

The E_1 (TO) mode of Zn-O at 410 cm^{-1} [39] is not seen in the current Raman spectrum, but this mode can be seen in the FTIR spectrum. The A_1(LO) mode at 574 cm^{-1} was also missing, as reported by Calleja and Cardona, and this mode could not be detected at excitation wavelengths longer than 406.7 nm [44]. Additional features emerge in the Ca-doped ZnO Raman spectra. The peak at 279 cm^{-1} has been assigned to B_1^{high}-B_1^{low} mode, and the peak at 1090 cm^{-1} can be assigned to the combination of the A_1(LO) and A_1(TO) modes. A broad asymmetric mode at 1157 cm^{-1} depicts the contributions of $2A_1$(LO) and $2E_1$(LO) modes. Additional modes at 279 cm^{-1} were also ascribed to the host lattice defects. Dopant-relat-

ed defects can disrupt the selection rule and activate the silent mode [45].

3.4 Morphological and elemental analysis

Figure 5 shows the FESEM images of the Ca-doped ZnO nanoparticles annealed at 800 °C for 6 hours. Micrographs of all samples show dispersed crystallites and also reveal polycrystalline nature. FESEM shows that all grains are more or less spherical, and the grain boundaries are well separated. The EDAX pattern in **Figure 6** illustrates the presence of prime elements zinc, calcium, and oxygen along with carbon trace as contamination. This carbon trace element was detected through the use of carbon tape as the base on the sample holder. The elemental proportion corresponding to Zn, Ca, and O is in good agreement with permissible error.

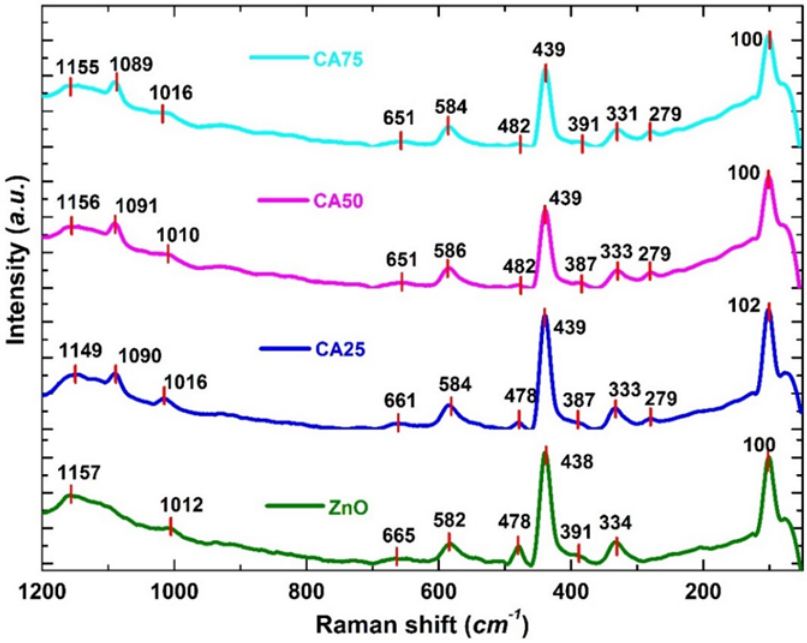

Figure 4. Raman spectra of pure ZnO and Ca-doped ZnO nanoparticles.

Table 2. Raman vibrational modes of ZnO and Ca-doped ZnO.

Sample	Wavenumber (cm^{-1})				PROCESS
ZnO	CA25	CA50	CA75	REFERENCE	
100	102	100	100	99 [39]	E_2^{low}
-	279	279	279	284 [39]	B_1^{high}-B_1^{low}
334	333	333	331	333 [39]	E_2^{high}-E_2^{low}
391	387	387	391	384 [41]	A_1(TO)
438	439	439	439	438 [39]	E_2^{high}
478	478	482	482	483 [39]	2LA
582	584	586	584	586 [41]	E_1(LO)
665	661	651	651	660 [41]	TA + LO
1012	1016	1010	1016	980 [41]	2TO
-	1090	1091	1089	1080 [44]	TO + LO
1157	1149	1156	1155	1158 [39]	$2A_1$(LO), $2E_1$(LO)

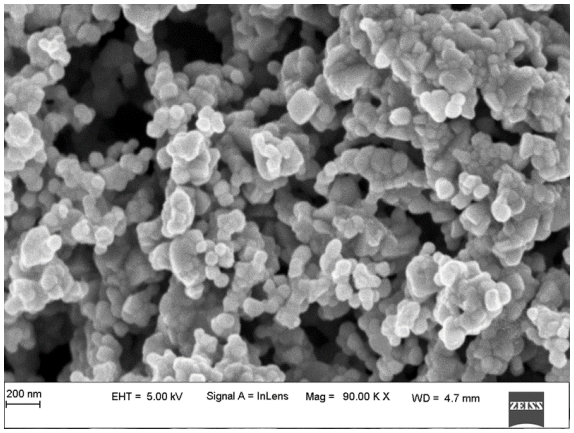

(a)

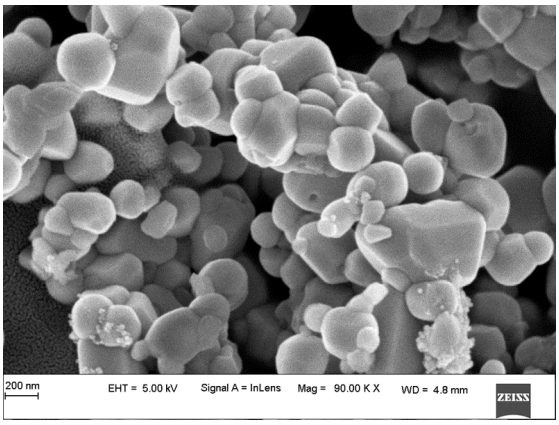

(b)

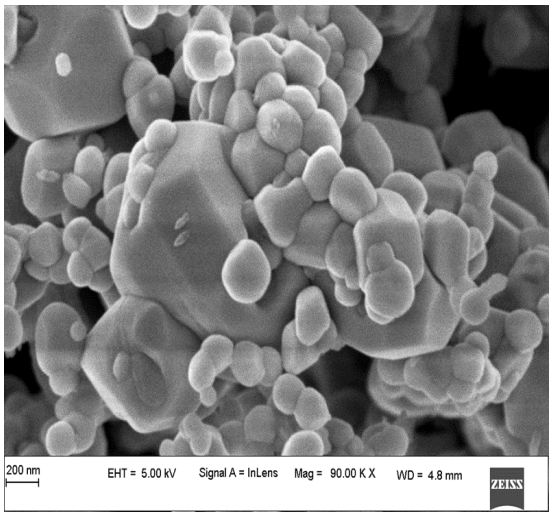

(c)

Figure 5. FESEM images of Ca-doped ZnO nanoparticles (a) $Zn_{0.975}Ca_{0.025}O$ (CA25), (b) $Zn_{0.95}Ca_{0.05}O$ (CA50) and (c) $Zn_{0.925}Ca_{0.075}O$ (CA75).

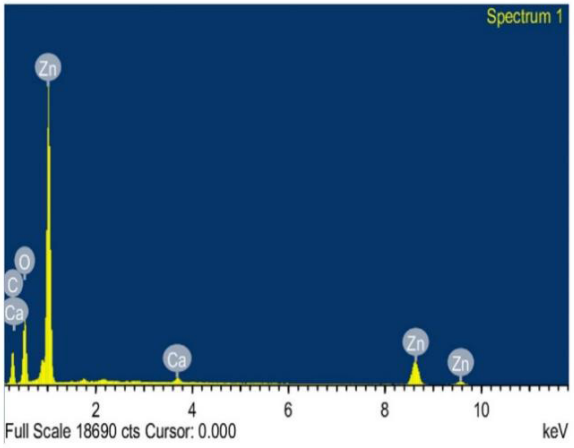

(a)

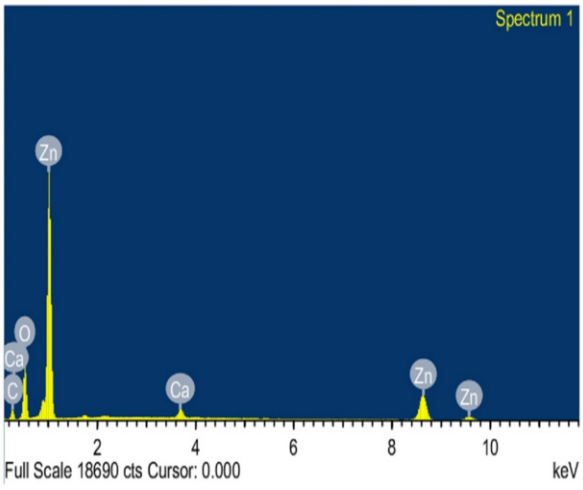

(b)

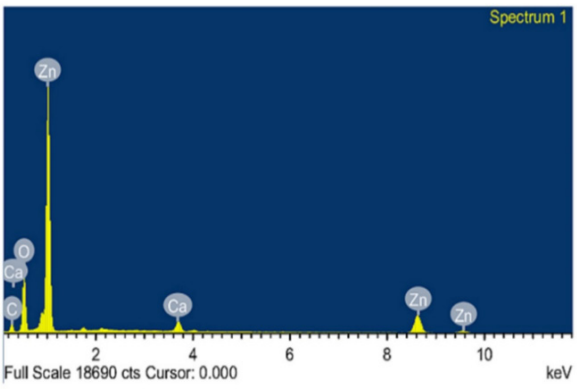

(c)

Figure 6. EDAX spectra of Ca-doped ZnO nanoparticles (a) $Zn_{0.975}Ca_{0.025}O$ (CA25), (b) $Zn_{0.95}Ca_{0.05}O$ (CA50) and (c) $Zn_{0.925}Ca_{0.075}O$ (CA75).

3.5 UV-Vis spectroscopy

Figure 7 shows the UV-Vis spectra of the ZnO and the calcium-doped ZnO samples. The absorption spectrum of pure and Ca-doped ZnO exhibits a strong absorption band at 369 nm due to its wide-bandgap energy. This indicates that the prepared samples were activated only under UV light irradiation. A characteristic absorption peak at about 369 nm can be assigned to the intrinsic bandgap absorption of ZnO due to the electronic transition from the valence band to the conduction band ($O_{2p} \rightarrow Zn_{3d}$) [15]. With increasing Ca concentration at the Zn sites, the samples exhibited a red shift of the absorption band and increased photoactivity. The Bandgap energy of the synthesized samples was determined using Tauc's relation:

$$ahv = A(hv - Eg)^{1/n} \quad (3)$$

where A is the constant of proportionality, h is Planck's constant, α is the absorption coefficient, υ is the optical frequency, and Eg is the energy bandgap. For direct bandgap semiconductors, n = 2. The bandgap energy was determined by plotting $(\alpha h\upsilon)^2$ versus photon energy $h\upsilon$. The undoped ZnO band gap energy is wider than the band gap energy (3.11 eV, FER = 1) in the work written by H. V. Vasei, et al. [46], which may be due to the use of different fuels during preparation. **Table 3** shows the band gap energy of the prepared samples. The band gap energy value from the Tauc plot (**Figure 8**) decreases from 3.24 eV to 3.22 eV with increasing Ca doping concentration. Morphology, size, and synthesis methods of ZnO nanoparticles are believed to influence the bandgap energy [47].

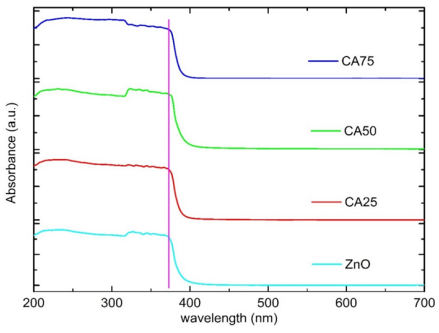

Figure 7. UV-vis absorption spectra of Pure and Ca-doped ZnO nanoparticles.

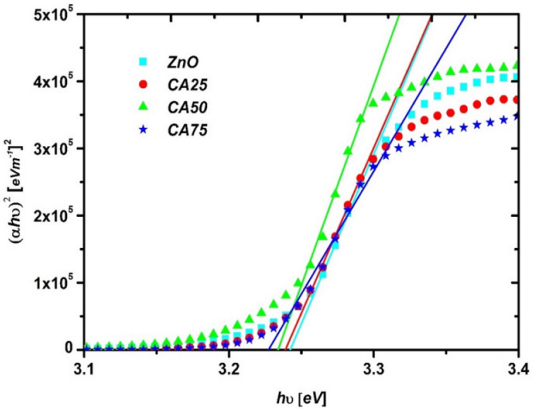

Figure 8. Tauc's plot of pure and Ca-doped ZnO nanoparticles.

Table 3. Bandgap energy of ZnO and Ca-doped ZnO.

Sample	**ZnO**	**CA25**	**CA55**	**CA75**
Band gap energy (*eV*)	3.242	3.238	3.231	3.227

3.6 Photoluminescence (PL) analysis

Figure 9 shows the photoluminescence spectra of pure ZnO and Ca-doped ZnO recorded at an excitation wavelength of 355 nm to determine excited states and defects. **Table 4** shows the emission bands of the prepared samples. The prepared nanoparticles exhibit four emission bands at 395 nm (band edge emission), 430 nm (violet emission), 490 nm (blue emission), and 515 nm, 580 nm (green emission). The UV emission near 395 nm, is attributed to direct exciton recombination resulting from near-band edge transitions in ZnO via an exciton-exciton process [48]. The emission of different visible colours represents the several intrinsic defects Vis Zn vacancies (V_{Zn}), O vacancies (V_0), Zn interstitials (Zn_i), O interstitials (O_i), and O anti-sites (O_{Zn}). The violet emission corresponds to the electron transitions from the shallow donor level of neutral Zni to the top of the valence band [49-51]. The blue emission is due to electron transfer from shallow donor levels of Zn interstitial atoms (Zn_i) to an acceptor level of neutral Zn vacancies (V_{Zn}) [52,53]. Green emission represents the radial recombination of photogenerated holes with electrons from the single-ionized oxygen (O) vacancies in the ZnO lattice surface. Furthermore, this is also due to radiative transitions between shallow donors (associated with O vacancies) and deep acceptors (Zn

vacancies) [54,55].

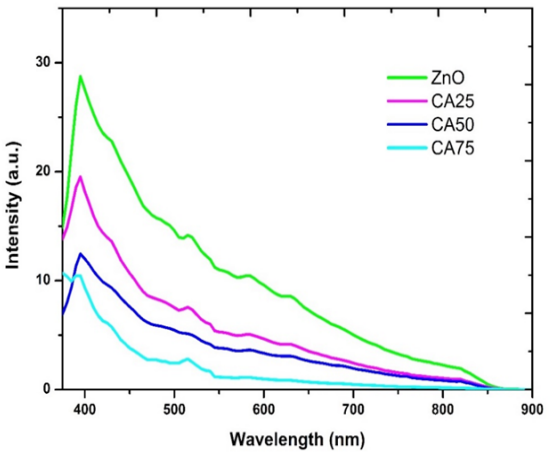

Figure 9. Photoluminescence emission spectra of pure and Ca-doped nanoparticles.

Table 4. Photoluminescence emission bands of ZnO and Ca-doped ZnO.

Sample Name	**Emission (nm)**				
ZnO	395	430	490	515	580
$Zn_{0.975}Ca_{0.025}O$	395	430	490	515	580
$Zn_{0.95}Ca_{0.05}O$	395	430	495	515	585
$Zn_{0.925}Ca_{0.075}O$	390	430	485	515	580
	UV	Violet	Blue	Green	Green

3.7 Impedance analysis

Impedance spectroscopy consists measurement of impedance Z as a function of frequency (υ). Sintered pellets coated with silver paint on both sides were used for impedance measurements. The impedance analyzer record the magnitude of the impedance |Z| and phase angle θ at various frequencies. Real (Z′) and imaginary (Z″) parts of the complex impedance ($Z^* = Z' + j\,Z''$) were calculated using $Z' = |Z| \cos\theta$ and $Z'' = |Z| \sin\theta$.

Figure 10 shows impedance spectra or Cole-Cole plots consisting of the real parts (Z′) and imaginary (Z″) parts of the complex impedance of the prepared samples. The Cole-Cole plots provide information on the resistance offered by the grain interior (G), grain boundary (GB), and electrode-material interfaces to the conduction of the charge carriers. The impedance spectrum consists of two semicircles, one at a high-frequency region and another at mid or low frequencies. The high-frequency semicircle ascribed to grain (G), and the semicircle at low frequency represents the grain boundary (GB) contribution. Grain resistance (R_g) and resistance due to grain boundary (R_{gb}) were obtained by fitting *R-CPE* equivalent circuits using Zview2. The general expression for the impedance of a constant phase element (*CPE)* is $Z_{CPE} = 1/Q(j\omega)^n$, where Q is the constant phase element (CPE), $j = \sqrt{-1}$ and ω is the angular frequency(ω = 2πυ, υ-frequency). When n = 1, Q acts as ideal capacitance C. The solid line represents the fit to the experimental data based on the equivalent circuit ($R_g||Q_g$) ($R_{gb}||Q_{gb}$) by Zview2. The total resistance (R_t) to the ion conduction is $R_t = R_g + R_{gb}$. The total conductivity of the samples was calculated using $\sigma_t = t/R_tA$. Where t is the pellet thickness, A is the pellet area, and R_t is the total resistance. **Table 5** consists of the fitted resistance values, the calculated grain conductivity ($\sigma_g = t/R_gA$), grain boundary conductivity ($\sigma_{gb} = t/R_{gb}A$), and total conductivity. Capacitors or CPEs in the *pF* range reflect grain interiors, and the *nF* range reflects grain boundaries. The grain resistance decreases with increasing the Ca doping concentration, similar to the results obtained by Irshad Ahmad et al. [48], whereas the grain boundary resistance increases with increasing Ca doping. **Figure 11** shows the variation of conductivity with dopant (Ca) concentration. It observed that there is an increase in grain conductivity with increasing doping because there is an increase of the charge carriers with increasing calcium doping [56]. On the other hand, the grain boundary conductivity decrease with increasing Ca doping. This is due to the precipitation of calcium at the ZnO grain boundaries, which calcifies the grain boundaries [57] and reduces the overall conductivity.

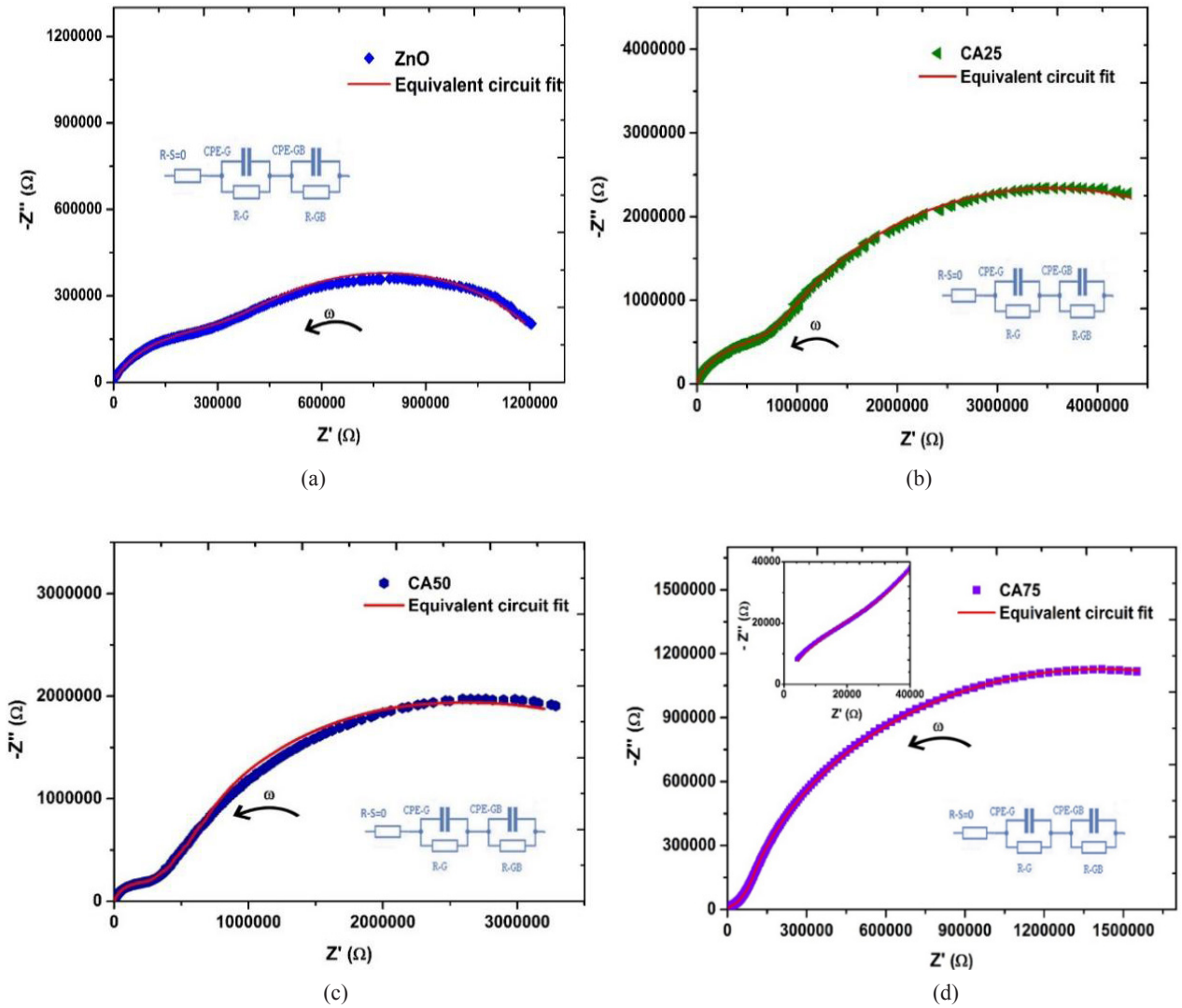

Figure 10. Impedance spectra or Cole-Cole plot of pure and Ca doped ZnO pellets sintered at 700 °C (a) ZnO (CA00), (b) $Zn_{0.975}Ca_{0.025}O$ (CA25), (c) $Zn_{0.95}Ca_{0.05}O$ (CA50) and (d) $Zn_{0.925}Ca_{0.075}O$ (CA75).

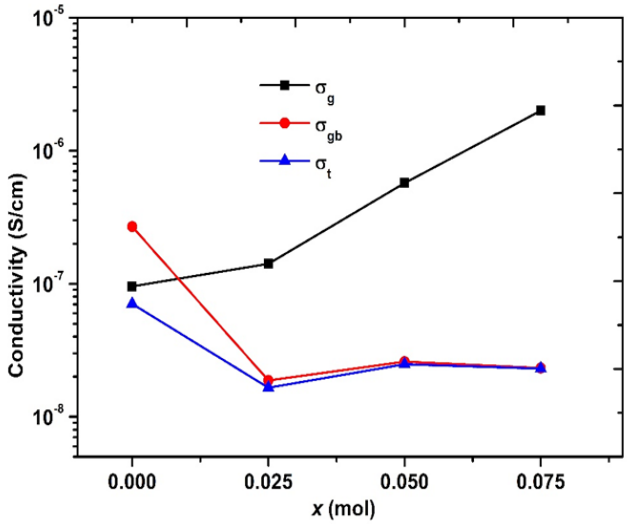

Figure 11. Variation of conductivity with dopant concentration.

Table 5. Impedance analysis results: Grain resistance (R_g), grain boundary resistance (R_{gb}), total resistance (R_t) and the calculated grain conductivity (σ_g), grain boundary conductivity (σ_{gb}) and total conductivity (σ_t).

Sample	R_g (ohm)	R_{gb} (ohm)	R_t (ohm)	σ_g (S/cm)	σ_{gb} (S/cm)	σ_t (S/cm)
ZnO	961430	341830	1303260	9.56×10^{-8}	2.69×10^{-7}	7.05×10^{-8}
CA25	746390	5629800	6376190	1.41×10^{-7}	1.87×10^{-8}	1.65×10^{-8}
CA50	194240	4278300	4472540	5.71×10^{-7}	2.59×10^{-8}	2.48×10^{-8}
CA75	31659	2722400	2754060	2.00×10^{-6}	2.33×10^{-8}	2.30×10^{-8}

4. Conclusions

The pure and Ca-doped ZnO nanoparticles were successfully prepared by the solution combustion technique. XRD investigations confirmed that the prepared samples had a hexagonal wurtzite structure without heterogeneous phases. XRD analysis also shows structural changes with Ca concentration, both in terms of lattice parameter and crystallite size. FESEM images show that the particles are nearly spherical and have few aggregates. EDX analysis identified the chemical composition of the prepared samples. The Raman spectrum depicts the hexagonal wurtzite structure of the ZnO, indicating the first and second-order active modes of the ZnO. The presence of wurtzite structural defects in the prepared samples was identified using PL spectroscopy. The decrease in optical bandgap is due to the increase in carrier concentration in Ca-doped ZnO nanoparticles, which increases the grain conductivity of the Ca-doped samples. The red shift of the energy bandgap and increase in grain conductivity suggests that Ca-doped ZnO is a potential candidate for photocatalytic applications.

Author Contributions

K. N. Ganesha: Conceptualization, data collection, analysis, investigation, methodology, writing—original draft; H. Chandrappa: Resources and feedback; S. R. Kumarswamy: Resources and critical feedback; V. Annadurai: Resources and critical feedback; H. Somashekarappa: Conceptualization, Supervision, validation, visualization, writing—review and editing; R. Somashekar: Conceptualization, validation, visualization, writing—review and editing.

Conflict of Interest

There is no conflict of interest.

Acknowledgement

The authors thank the Department of Collegiate Education, Government of Karnataka providing a grant to purchase equipment for sample preparation. The authors acknowledge the DST-PURSE laboratory at Mangalagangotri, Mangalore University, facilitating the XRD, FESEM, and EDX characterization facility. The authors thank SAIF, IITM, Chennai, for FTIR and UV-VIS characterization facilities. Authors acknowledge IOE, University of Mysore, Manasagangotri, Mysore 570 006, India facilitating Raman and Impedance analyzer.

References

[1] Chao, J., Chen, Y., Xing, S., et al., 2019. Facile fabrication of ZnO/C nanoporous fibers and ZnO hollow spheres for high performance gas sensor. Sensors and Actuators B: Chemical. 298, 126927.
DOI: https://doi.org/10.1016/j.snb.2019.126927

[2] Franco, M.A., Conti, P.P., Andre, R.S., et al., 2022. A review on chemiresistive ZnO gas sensors. Sensors and Actuators Reports. 4, 100100.
DOI: https://doi.org/10.1016/j.snr.2022.100100

[3] Kulkarni, D.R., Malode, S.J., Prabhu, K.K., et al.,

2020. Development of a novel nanosensor using Ca-doped ZnO for antihistamine drug. Materials Chemistry and Physics. 246, 122791.
DOI: https://doi.org/10.1016/j.matchemphys.2020.122791

[4] Alshammari, A.S., Khan, Z.R., Gandouzi, M., et al., 2022. Tailoring the optical properties and the UV detection performance of sol-gel deposited ZnO nanostructured thin films via Cd and Na co-doping. Optical Materials. 126, 112146.
DOI: https://doi.org/10.1016/j.optmat.2022.112146

[5] Li, L.E., Demianets, L.N.. 2008. Room-temperature excitonic lasing in ZnO tetrapod-like crystallites. Optical Materials. 30(7), 1074-1078.
DOI: https://doi.org/10.1016/j.optmat.2007.05.013

[6] Pandey, R.K., Dutta, J., Brahma, S., et al., 2021. Review on ZnO-based piezotronics and piezoelectric nanogenerators: Aspects of piezopotential and screening effect. Journal of Physics: Materials. 4(4), 044011.
DOI: https://dx.doi.org/10.1088/2515-7639/ac130a

[7] Sahoo, R., Mishra, S., Ramadoss, A., et al., 2020. An approach towards the fabrication of energy harvesting device using Ca-doped ZnO/PVDF-TrFE composite film. Polymer. 205, 122869.
DOI: https://doi.org/10.1016/j.polymer.2020.122869

[8] Liu, J., Wang, Y., Ma, J., et al., 2019. A review on bidirectional analogies between the photocatalysis and antibacterial properties of ZnO. Journal of Alloys and Compounds. 783, 898-918.
DOI: https://doi.org/10.1016/j.jallcom.2018.12.330

[9] Kim, I., Viswanathan, K., Kasi, G., et al., 2022. ZnO nanostructures in active antibacterial food packaging: Preparation methods, antimicrobial mechanisms, safety issues, future prospects, and challenges. Food Reviews International. 38(4), 537-565.
DOI: https://doi.org/10.1080/87559129.2020.1737709

[10] Kumar, R., Umar, A., Kumar, G., et al., 2017. Antimicrobial properties of ZnO nanomaterials: A review. Ceramics International. 43(5), 3940-3961.
DOI: https://doi.org/10.1016/j.ceramint.2016.12.062

[11] Hameed, A., Fatima, G.R., Malik, K., et al., 2019. Scope of nanotechnology in cosmetics: Dermatology and skin care products. Journal of Medicinal Chemical Science. 2(1), 9-16.
DOI: https://doi.org/10.26655/jmchemsci.2019.6.2

[12] Safdar, M., Waqas, M., Jabeen, N., et al., 2022. Fabrication of In_2Te_3 nanowalls garnished with ZnO nanoparticles and their field emission behavior. Materials Chemistry and Physics. 290, 126510.
DOI: https://doi.org/10.1016/j.matchemphys.2022.126510

[13] Özgür, Ü., Alivov, Y.I., Liu, C., et al., 2005. A comprehensive review of ZnO materials and devices. Journal of Applied Physics. 98(4), 11.
DOI: https://doi.org/10.1063/1.1992666

[14] Selvi, K.T., Mangai, K.A., Priya, M., et al., 2020. Investigation of the dielectric and impedance properties of ZnO/MgO nanocomposite. Physica B: Condensed Matter. 594, 412355.
DOI: https://doi.org/10.1016/j.physb.2020.412355

[15] Sulciute, A., Nishimura, K., Gilshtein, E., et al., 2021. ZnO nanostructures application in electrochemistry: Influence of morphology. The Journal of Physical Chemistry C. 125(2), 1472-1482.
DOI: https://doi.org/10.1021/acs.jpcc.0c08459

[16] Umavathi, S., AlSalhi, M.S., Devanesan, S., et al., 2020. Synthesis and characterization of ZnO and Ca-ZnO nanoparticles for potential antibacterial activity and plant micronutrients. Surfaces and Interfaces. 21, 100796.
DOI: https://doi.org/10.1016/j.surfin.2020.100796

[17] Mahajan, P., Singh, A., Arya, S., 2020. Improved performance of solution processed organic solar cells with an additive layer of sol-gel synthesized ZnO/CuO core/shell nanoparticles. Journal of Alloys and Compounds. 814, 152292.
DOI: https://doi.org/10.1016/j.jallcom.2019.152292

[18] Abed, C., Bouzidi, C., Elhouichet, H., et al., 2015. Mg doping induced high structural quality of sol-gel ZnO nanocrystals: Application in photocatalysis. Applied Surface Science. 349, 855-

863.
DOI: https://doi.org/10.1016/j.apsusc.2015.05.078

[19] Liu, S., Zhu, L., Cao, W., et al., 2021. Defect-related optical properties of Mg-doped ZnO nanoparticles synthesized via low temperature hydrothermal method. Journal of Alloys and Compounds. 858, 157654.
DOI: https://doi.org/10.1016/j.jallcom.2020.157654

[20] Suwanboon, S., Amornpitoksuk, P., Sukolrat, A., 2011. Dependence of optical properties on doping metal, crystallite size and defect concentration of M-doped ZnO nanopowders (M = Al, Mg, Ti). Ceramics International. 37(4), 1359-1365.
DOI: https://doi.org/10.1016/j.ceramint.2010.12.010

[21] Ahmad, F., Maqsood, A., 2021. Structural, electric modulus and complex impedance analysis of ZnO at low temperatures. Materials Science and Engineering: B. 273, 115431.
DOI: https://doi.org/10.1016/j.mseb.2021.115431

[22] Kuo, C.L., Wang, C.L., Ko, H.H., et al., 2010. Synthesis of zinc oxide nanocrystalline powders for cosmetic applications. Ceramics International. 36(2), 693-698.
DOI: https://doi.org/10.1016/j.ceramint.2009.10.011

[23] Hameed, A.S.H., Karthikeyan, C., Sasikumar, S., et al., 2013. Impact of alkaline metal ions Mg^{2+}, Ca^{2+}, $Sr2^{+}$ and Ba^{2+} on the structural, optical, thermal and antibacterial properties of ZnO nanoparticles prepared by the co-precipitation method. Journal of Materials Chemistry B. 1(43), 5950-5962.
DOI: http://dx.doi.org/10.1039/c3tb21068e

[24] Pathak, T.K., Kumar, A., Swart, C.W., et al., 2016. Effect of fuel content on luminescence and antibacterial properties of zinc oxide nanocrystalline powders synthesized by the combustion method. RSC Advances. 6(100), 97770-97782.
DOI: http://dx.doi.org/10.1039/C6RA22341A

[25] El Mir, L., 2017. Luminescence properties of calcium doped zinc oxide nanoparticles. Journal of Luminescence. 186, 98-102.
DOI: https://doi.org/10.1016/j.jlumin.2017.02.029

[26] Karthikeyan, B., Pandiyarajan, T., Mangaiyarkarasi, K., 2011. Optical properties of sol-gel synthesized calcium doped ZnO nanostructures. Spectrochimica Acta Part A: Molecular and Biomolecular Spectroscopy. 82(1), 97-101.
DOI: https://doi.org/10.1016/j.saa.2011.07.005

[27] Morales, A.E., Zaldivar, M.H., Pal, U., 2006. Indium doping in nanostructured ZnO through low-temperature hydrothermal process. Optical Materials. 29(1), 100-104.
DOI: https://doi.org/10.1016/j.optmat.2006.03.010

[28] Ilager, D., Malode, S.J., Kulkarni, R.M., et al., 2022. Electrochemical sensor based on Ca-doped ZnO nanostructured carbon matrix for algicide dichlone. Journal of Hazardous Materials Advances. 7, 100132.
DOI: https://doi.org/10.1016/j.hazadv.2022.100132

[29] Ilager, D., Shetti, N.P., Malladi, R.S., et al., 2021. Synthesis of Ca-doped ZnO nanoparticles and its application as highly efficient electrochemical sensor for the determination of anti-viral drug, acyclovir. Journal of Molecular Liquids. 322, 114552.
DOI: https://doi.org/10.1016/j.molliq.2020.114552

[30] Jaballah, S., Benamara, M., Dahman, H., et al., 2020. Formaldehyde sensing characteristics of calcium-doped zinc oxide nanoparticles-based gas sensor. Journal of Materials Science: Materials in Electronics. 31, 8230-8239.
DOI: https://doi.org/10.1007/s10854-020-03358-y

[31] Varma, A., Mukasyan, A.S., Rogachev, A.S., et al., 2016. Solution combustion synthesis of nanoscale materials. Chemical Reviews. 116(23), 14493-14586.
DOI: https://doi.org/10.1021/acs.chemrev.6b00279

[32] Cheruku, R., Vijayan, L., Govindaraj, G., 2012. Electrical relaxation studies of solution combustion synthesized nanocrystalline Li_2NiZrO_4 material. Materials Science and Engineering: B. 177(11), 771-779.
DOI: https://doi.org/10.1016/j.mseb.2012.04.005

[33] Jain, S.R., Adiga, K.C., Verneker, V.P., 1981. A new approach to thermochemical calculations of condensed fuel-oxidizer mixtures. Combustion

and Flame. 40, 71-79.
DOI: https://doi.org/10.1016/0010-2180(81)90111-5

[34] Pathak, L.C., Singh, T.B., Das, S., et al., 2002. Effect of pH on the combustion synthesis of nano-crystalline alumina powder. Materials Letters. 57(2), 380-385.
DOI: https://doi.org/10.1016/S0167-577X(02)00796-6

[35] Scherrer, P., 1918. Bestimmung der Grösse und der inneren Struktur von Kolloidteilchen mittels Röntgenstrahlen (German) [Determination of the size and internal structure of colloidal particles using X-rays]. Nachr. Ges. Wiss. Göttingen. 26, 98-100.

[36] Cheng, B., Xiao, Y., Wu, G., et al., 2004. The vibrational properties of one-dimensional ZnO: Ce nanostructures. Applied Physics Letters. 84(3), 416-418.
DOI: https://doi.org/10.1063/1.1639131

[37] Vergés, M.A., Mifsud, A., Serna, C.J., 1990. Formation of rod-like zinc oxide microcrystals in homogeneous solutions. Journal of the Chemical Society, Faraday Transactions. 86(6), 959-963.
DOI: http://dx.doi.org/10.1039/FT9908600959

[38] Sigoli, F.A., Davolos, M.R., Jafelicci Jr, M., 1997. Morphological evolution of zinc oxide originating from zinc hydroxide carbonate. Journal of Alloys and Compounds. 262, 292-295.
DOI: https://doi.org/10.1016/S0925-8388(97)00404-0

[39] Cuscó, R., Alarcón-Lladó, E., Ibanez, J., et al., 2007. Temperature dependence of Raman scattering in ZnO. Physical Review B. 75(16), 165202.
DOI: https://doi.org/10.1103/PhysRevB.75.165202

[40] Damen, T.C., Porto, S.P.S., Tell, B., 1966. Raman effect in zinc oxide. Physical Review. 142(2), 570.
DOI: https://doi.org/10.1103/PhysRev.142.570

[41] Šćepanović, M.G.B.M., Grujić-Brojčin, M., Vojisavljević, K., et al., 2010. Raman study of structural disorder in ZnO nanopowders. Journal of Raman Spectroscopy. 41(9), 914-921.
DOI: https://doi.org/10.1002/jrs.2546

[42] Rosset, A., Djessas, K., Goetz, V., et al., 2020. Sol-gel synthesis and solar photocatalytic activity of Ca-alloyed ZnO nanoparticles elaborated using different precursors. RSC Advances. 10(43), 25456-25466.
DOI: http://dx.doi.org/10.1039/C9RA10131D

[43] Xing, Y.J., Xi, Z.H., Xue, Z.Q., et al., 2003. Optical properties of the ZnO nanotubes synthesized via vapor phase growth. Applied Physics Letters. 83(9), 1689-1691.
DOI: https://doi.org/10.1063/1.1605808

[44] Calleja, J.M., Cardona, M., 1977. Resonant raman scattering in ZnO. Physical Review B. 16(8), 3753.
DOI: https://link.aps.org/doi/10.1103/PhysRevB.16.3753

[45] Bundesmann, C., Ashkenov, N., Schubert, M., et al., 2003. Raman scattering in ZnO thin films doped with Fe, Sb, Al, Ga, and Li. Applied Physics Letters. 83(10), 1974-1976.
DOI: https://doi.org/10.1063/1.1609251

[46] Vasei, H.V., Masoudpanah, S.M., Habibollahzadeh, M., 2020. Different morphologies of ZnO via solution combustion synthesis: The role of fuel. Materials Research Bulletin. 125, 110784.
DOI: https://doi.org/10.1016/j.materresbull.2020.110784

[47] Agarwal, S., Jangir, L.K., Rathore, K.S., et al., 2019. Morphology-dependent structural and optical properties of ZnO nanostructures. Applied Physics A. 125, 1-7.
DOI: https://doi.org/10.1007/s00339-019-2852-x

[48] Ahmad, I., Ahmed, E., Ahmad, M., et al., 2020. The investigation of hydrogen evolution using Ca doped ZnO catalysts under visible light illumination. Materials Science in Semiconductor Processing. 105, 104748.
DOI: https://doi.org/10.1016/j.mssp.2019.104748

[49] Pascariu, P., Tudose, I.V., Suchea, M., et al., 2018. Preparation and characterization of Ni, Co doped ZnO nanoparticles for photocatalytic applications. Applied Surface Science. 448, 481-488.
DOI: https://doi.org/10.1016/j.apsusc.2018.04.124

[50] Kumar, A.S., Huang, N.M., Nagaraja, H.S.,

2014. Influence of Sn doping on photoluminescence and photoelectrochemical properties of ZnO nanorod arrays. Electronic Materials Letters. 10, 753-758.
DOI: https://doi.org/10.1007/s13391-014-3348-7

[51] Mishra, S.K., Srivastava, R.K., Prakash, S.G., et al., 2010. Photoluminescence and photoconductive characteristics of hydrothermally synthesized ZnO nanoparticles. Opto-Electronics Review. 18(4), 467-473.
DOI: https://doi.org/10.2478/s11772-010-0037-4

[52] Wu, C., Shen, L., Zhang, Y.C., et al., 2011. Solvothermal synthesis of Cr-doped ZnO nanowires with visible light-driven photocatalytic activity. Materials Letters. 65(12), 1794-1796.
DOI: https://doi.org/10.1016/j.matlet.2011.03.070

[53] Umar, A., Ribeiro, C., Al-Hajry, A., et al., 2009. Growth of highly c-axis-oriented ZnO nanorods on ZnO/glass substrate: Growth mechanism, structural, and optical properties. The Journal of Physical Chemistry C. 113(33), 14715-14720.
DOI: https://doi.org/10.1021/jp9045098

[54] Umar, A., Hahn, Y.B., 2006. ZnO nanosheet networks and hexagonal nanodiscs grown on silicon substrate: Growth mechanism and structural and optical properties. Nanotechnology. 17(9), 2174.
DOI: https://dx.doi.org/10.1088/0957-4484/17/9/016

[55] Dai, Y., Zhang, Y., Bai, Y.Q., et al., 2003. Bicrystalline zinc oxide nanowires. Chemical Physics Letters. 375(1-2), 96-101.
DOI: https://doi.org/10.1016/S0009-2614(03)00823-6

[56] Saadi, H., Rhouma, F.I.H., Benzarti, Z., et al., 2020. Electrical conductivity improvement of Fe doped ZnO nanopowders. Materials Research Bulletin. 129, 110884.
DOI: https://doi.org/10.1016/j.materresbull.2020.110884

[57] Zhao, H., Wang, H., Meng, X., et al., 2021. A method to reduce ZnO grain resistance and improve the intergranular layer resistance by Ca^{2+} and Al^{3+} co-doping. Materials Science in Semiconductor Processing. 128, 105768.
DOI: https://doi.org/10.1016/j.mssp.2021.105768